## Revealing the effect of interstitial oxygen on the low-energy crystal electric field excitations of Pr<sup>3+</sup> in 214-nickelates

Rajesh Dutta, <sup>1,2,\*</sup> Avishek Maity, <sup>3,†</sup> Anna Marsicano, <sup>4</sup> J. Ross Stewart, <sup>5</sup> Matthias Opel, <sup>6</sup> and Werner Paulus <sup>4</sup>

<sup>1</sup> Institut für Kristallographie, RWTH Aachen Universität, 52066 Aachen, Germany

<sup>2</sup> Jülich Centre for Neutron Science at Heinz Maier-Leibnitz Zentrum, 85747 Garching, Germany

<sup>3</sup> Heinz Maier-Leibnitz Zentrum, Technische Universität München, 85747 Garching, Germany

<sup>4</sup> Institut Charles Gerhardt Montpellier, Université de Montpellier, 34095 Montpellier, France

<sup>5</sup> ISIS Neutron and Muon Source, Rutherford Appleton Laboratory, Didcot OX11 0QX, United Kingdom

<sup>6</sup> Walther-Meißner-Institut, Bayerische Akademie der Wissenschaften, 85748 Garching, Germany

We report an inelastic neutron scattering study (INS) on the low-energy crystal electric field (CEF) excitations of  $\Pr_{2-x} \operatorname{Sr}_x \operatorname{NiO}_{4+\delta}$  single crystals at various temperature. The observed low-E CEF level of the O-doped sample ( $x=0,\delta\approx0.24$ ) at  $\sim5.5$  meV appears at significantly lower energy than that of the Sr-doped sample ( $x=0.5,\delta=0.0$ ) at  $\sim8.5$  meV. Applying the point charge (PC) model calculation this has been interpreted as an effect of the interstitial oxygen via lowering the local symmetry and modifying the CEF environment of the central rare earth  $\Pr^{3+}$  ( $^3H_4$ ) ions.

I. Introduction: Complex oxides in the family of 11 strongly correlated electron systems involving both  $4f^n$  $_{12}$  lanthanide and  $3d^n$  transition metal ions exhibit a rich variety of novel phenomena due to a combination of their 14 electronic interactions of spin, orbital and charge de-<sub>15</sub> grees of freedom [1–4]. 214-nickelates, cobaltates and 16 cuprates fall into these similar categories and their mag-17 netism either Néel or stripe antiferromagnetic (AFM) 18 differs depending on the corresponding spin states of  $_{19}$  the divalent transition metal (TM) ions  $\mathrm{Ni}^{2+}$  (S = 1),  $_{20}$  Co<sup>2+</sup> (S = 3/2) and Cu<sup>2+</sup> (S = 1/2), respectively [5-8]. 21 The underlying magnetism becomes more complicated 22 by the presence of magnetic trivalent lanthanide (Ln)23 ions (Ln = Pr, Nd, Sm) in comparison to the nonmag-<sup>24</sup> netic La<sup>3+</sup> [9–11]. In some cases the polarizing effect  $_{25}$  i.e. the internal magnetic fields acting on the Ln sites 26 induced by the ordered magnetic moment of the TM ions 27 or vice versa, plays an active role determining the mi-28 croscopic electronic and magnetic ground state [12–14]. Despite such polarization,  $Ln^{3+}$  posses unique single-ion 30 like character defined by the local CEF which splits the  $_{31}$   $4f^n$  electronic states into a series of energy levels deter-32 mining the overall magnetic and physical properties of 33 the system. The CEF potential contains crucial infor-34 mation on the local electronic structure and the ground 35 state of the system.

Studies of the parent  $(Nd,Pr)_2NiO_4$  show that the Kramers  $Nd^{3+}$  ions start to order antiferromagnetically below 10 K with magnetic moment  $(3.2\mu_B)$  at 1.5 K while the non-Kramers  $Pr^{3+}$  ions order partially or remain almost in paramagnetic singlet ground state even below 1.5 K [15, 16]. There are differences as well in the CEF excitations with doping. In both, parent and doped (Sr = 0.4) Nd-nickelates, the lowest CEF excitation of  $Nd^{3+}$  has been observed almost at same energy ( $\sim 8 \text{ meV}$ ) [17], while the lowest CEF excitation in the parent  $Pr_2NiO_4$  has been reported at  $\sim 4.3 \text{ meV}$  [18]. However,  $Pr^{3+}$  and  $Nd^{3+}$  ions differ from each other to a greater extent in terms of  $4f^n$  splitting by the CEF and

<sup>49</sup> the polarizing effect by the ordered Ni<sup>2+</sup> spin sublattice.
<sup>50</sup> Nonetheless, to our knowledge, so far there have been
<sup>51</sup> no further studies on the Sr/O-doped Pr-nickelates re<sup>52</sup> porting on low energy CEF excitations. Therefore, it is
<sup>53</sup> important to investigate the CEF excitations of Sr/O<sup>54</sup> doped Pr-nickelates to understand the cooperative in<sup>55</sup> terplay of electronic correlations of Pr<sup>3+</sup> under different
<sup>56</sup> CEF potentials due to different types of doping.

In this article, we present a detailed study of 58 the CEF excitations of  $Pr_{1.5}Sr_{0.5}NiO_4$  (PSNO) and  $_{59}~\mathrm{Pr_2NiO_{4.24\pm0.01}}$  (PNO) single crystals, both of which lie 60 at the higher doping sides of Pr<sub>2</sub>NiO<sub>4</sub> with an electroni-61 cally equivalent doping concentration  $(n_h = x + 2\delta)$ , es-62 pecially showing the effect of interstitial oxygen  $(O_{int})$ <sub>63</sub> on the Pr<sup>3+</sup> CEF excitations in comparison with Sr-64 doping by looking at low energy INS spectra. However, 65 the Sr- and O-doped compounds do not align apparently 66 in terms of the crystal field environment and the elec-<sub>67</sub> tronic states of the localized Pr<sup>3+</sup> ion. We have used PC 68 model simulation incorporating the local CEF environ-69 ment in both compounds to explain the observed CEF 70 excitation of Pr<sup>3+</sup> and the models are verified against the directionally dependent magnetic susceptibility and 72 magnetization curves. Interestingly, in the case of the PNO sample, incorporating excess  $O_{int}$ , nominally one 74 per unit cell, lowers the local symmetry of those particular Pr atoms close to the  $O_{int}$  resulting in different crystal field splitting compared to those Pr atoms without a nearby  $O_{int}$ . Our study indicates the impor-78 tance of including the actual CEF environment in the 79 PC modelling in order to describe the related single-ion 80 properties.

II. METHODS: We have used the single crystals of PSNO and PNO taken for our previous studies [19–21] and the INS experiments are performed on the thermal triple-axis spectrometer (TAS) PUMA [22] at Heinz Maier-Leibnitz Zentrum, Germany and on the thermal neutron time-of-flight (TOF) chopper spectrometer MAPS [23] at the ISIS Neutron and Muon Source of the Rutherford Appleton Laboratory, UK. The details of the experimental methods are described in references [19–21]. Additional macroscopic magnetic measurements on both samples have been performed using a supercon-

<sup>\*</sup> Corresponding author: rajesh.dutta@frm2.tum.de

<sup>&</sup>lt;sup>†</sup> Corresponding author: avishek.maity@frm2.tum.de

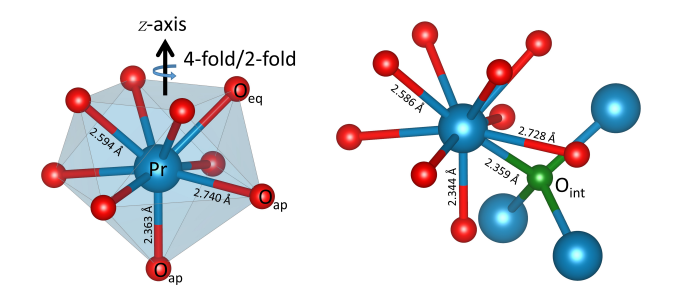


FIG. 1. (Left) Capped-square antiprism CEF environment of  $\Pr^{3+}$  ion with 4-fold or 2-fold rotational z-axis (black arrow) of the local point symmetry in case of 4/mmm or mmm, respectively. (Right) CEF environment with an extra  $O_{int}$  (green).

92 ducting quantum interference device (SQUID) magne-93 tometer under DC mode (MPMS XL7-Quantum Design 94 Inc., San Diego, CA) at the Walther-Meißner-Institut, 95 Germany.

III. RESULTS AND DISCUSSION: PSNO (mass = 597 g) crystallizes in tetragonal structure with space group <sub>98</sub> I4/mmm and lattice parameters a=3.78 Å, c=12.54<sup>99</sup> Å where the onset of the Ni<sup>2+</sup> spin-stripe ordering takes 100 place below 130 K whereas for PNO it takes place al-101 most at room temperature (RT) but start to become pronounced below  $\approx 220$  K. PNO (mass = 3.5 g) crys-103 tallizes in a monoclinic structure adopting space group F112/m and lattice parameters a = 5.39 Å, b = 5.45 Å, $_{105}$  c = 12.44 Å,  $\gamma = 90.03^{\circ}$ . The monoclinic symmetry im-106 plies an additional complexity related to twin domains as further outlined in the references [24, 25]. This leads 108 to a pseudomerohedrical overlay of satellite reflections 109 related to the only small deviation from an orthorhombic 110 symmetry (Fmmm) as the monoclinic angle is 90.03°. 111 However, the established long range O-ordering will cer-112 tainly imply a well defined atomic positions even though 113 of low point symmetry of Pr. Since the deviation from an orthorhombic symmetry is only minor, we have cho-115 sen the respective Fmmm unit cell for theoretical PC modelling. This turned out to be still a good choice, although the real point symmetry is supposed to be lower.

Figure 1 shows only the Pr-polyhedra in both cases 118 of doping. In the PSNO, Pr<sup>3+</sup> ions have capped-square 120 antiprism-type coordination by three sets of non-equal 121 Pr-O bonds and are kept at a long distance in the 122 structure not being influenced by the ordered magnetic 123 moments of the Ni<sup>2+</sup> sublattice. However, in case of  $_{124}$  PNO with Fmmm setting as there will be one  $O_{int}$  in 125 the unit cell occupying any of the eight possible Wyckoff position 8f(1/4,1/4,1/4), we have to consider two sets of Pr-polyhedra, one with a nearby  $O_{int}$  and other without the nearby  $O_{int}$ . Using these structural input we have carried out PC calculations using PyCrystal-FIELD software [26] to simulate the experimental neu-130 tron spectrum and SQUID data. 131

In order to describe the experimental observation we start with building the CEF Hamiltonian from Coulombic repulsion for the PC calculation treating the surrounding ligands (O) as point charges (2e) and the

136 Hamiltonian can be written as

$$\mathcal{H}_{CEF} = \sum_{n,m} B_n^m O_n^m, \tag{1}$$

 $_{\mbox{\tiny 137}}$  where  $B^m_n$  are so-called CEF parameters and  $O^m_n$  are the Stevens Operators with  $-n \ge m \ge n$ . In general for the  $_{139}$  rare earth (RE) ion, 4f electrons are more shielded from  $_{140}$  their ligands than 3d TM electrons, leaving the crystal 141 field weak compared to the spin-orbit interaction. Thus J becomes a good quantum number in RE ions. For our calculation we stick to the J-basis for  $Pr^{3+}$ . To have non-zero CEF parameters of the central ion and to eliminate the imaginary CEF operators one needs to 146 find the y-axis normal to the mirror plane and the z-axis 147 along the highest rotation axis. In the tetragonal case 148 of PSNO the z-axis lies along the 4-fold rotation axis of 149 the crystal structure (left in Fig. 1). But in PNO, we have two different CEF environments: one without  $O_{int}$ where the z-axis is along 2-fold rotation axis (similar 152 to left in Fig. 1) and the other with  $O_{int}$  where the  $_{153}$  corresponding high-symmetry z-axis is absent but the 154 y-axis perpendicular to the diagonal (110) mirror plane 155 passing through  $O_{int}$ .

We start with the discussion of results from the PSNO sample followed by the comparison with the results from PNO sample. Two-dimensional (2D) energy-momentum  $_{159}$  (E-Q) maps and the corresponding one-dimensional

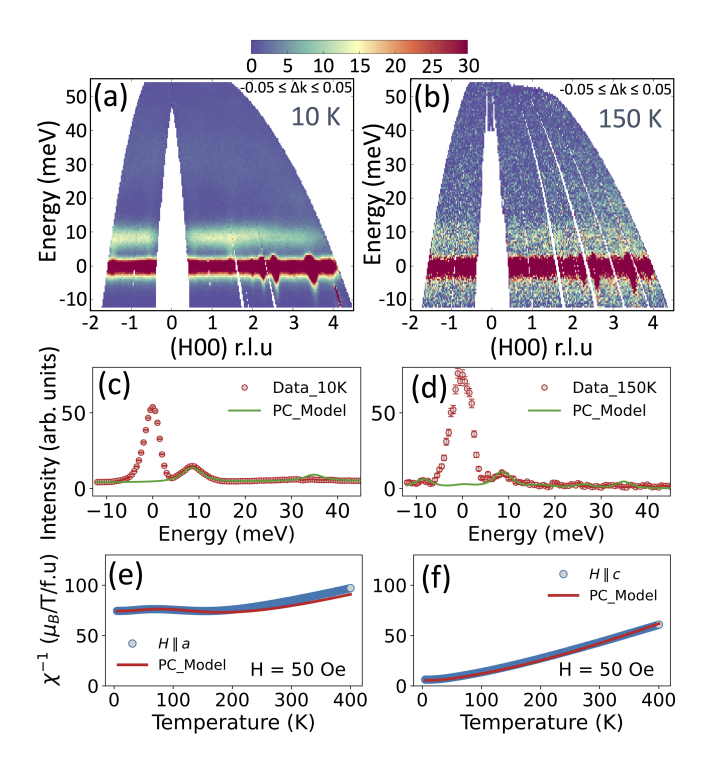
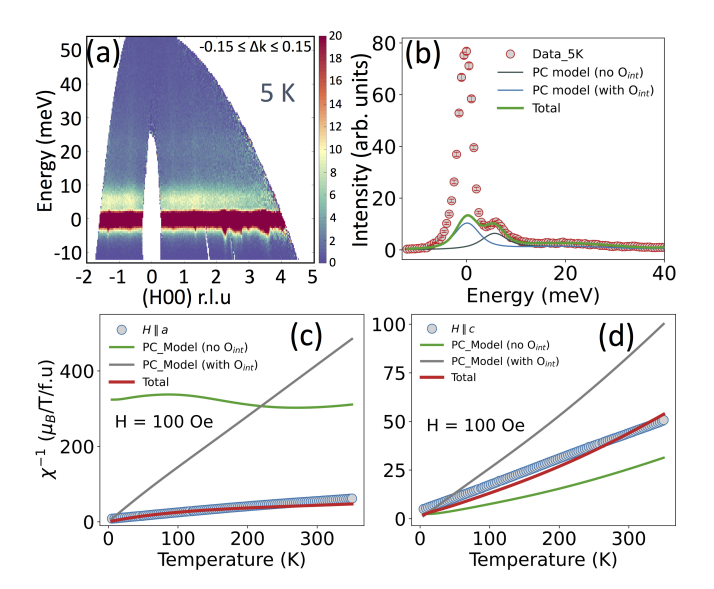


FIG. 2. The INS spectra of PSNO measured at MAPS spectrometer with incident neutron energy  $E_i = 60$  meV at (a) 10 K and (b) 150 K. Corresponding 1D line cuts at (100) with  $0.95 \le \Delta h \le 1.05$  (r.l.u) are shown in (c,d) with vertical error bars, where the solid green lines represent the calculated CEF excitations from the PC model. Inverse magnetic susceptibility along the crystallographic (e) a- and (f) c-axis where the solid red lines are the calculated inverse susceptibility of  $Pr^{3+}$  using PC model.

160 (1D) line cuts of excitation spectra of PSNO are shown 161 in Fig. 2(a,b) and (c,d) respectively. These line cuts 162 were chosen in such a way that they do not include any 163 elastic signal from the spin stripe ordering and nuclear Bragg peaks. Thus intensity at E = 0 meV is solely 165 coming from incoherent scattering as there is no inten-166 sity expected from the calculation for the ground state 167 CEF of  $Pr^{3+}$  at low-T. The low lying CEF excitations  $_{168}$  apears at  $\sim 8.85$  meV with a broad full-width at half  $_{169}$  maxima (FWHM)  $\sim 5.5$  meV where the instrumental 170 resolution is only 2.8 - 3 meV.  $Pr^{3+}$  ion with  $4f^2$  elec-171 tron has quantum numbers S = 1, L = 5 giving rise to  $_{172}$  an effective J=4 by Hund's rule and under the CEF 173 it splits the electronic states into two doublets and five  $_{174}$  singlets for  $d_{4h}$  symmetry. In this configuration we have 175 5 non-zero  $B_n^m$  CEF parameters namely  $B_2^0$ ,  $B_4^0$ ,  $B_4^4$ , 176  $B_6^0$  and  $B_6^4$  which are given in the Table I considering effective oxygen charge to be 2e. We found these  $B_n^m$  pa-178 rameters are almost robust even if we consider the effec-179 tive oxygen charge to be 1.7e [see the Table I]. However,  $_{180}$  the second excited doublets predicted at 34.85 meV was 181 difficult to identify because of the weak and broad in-182 tensity distribution of the spectra in this energy range  $_{183}$  of 25 to 40 meV (as visible in the color map in Fig. 2 184 (a)) which includes contribution as well from magnons 185 [20]. Rest of the eigenvalues show no intensity in the PC 186 model calculation similar to the experimental data. As 187 we have found only one strong CEF excitations in the 188 INS spectrum measured up to 54 meV and we have five 189 CEF parameters, we avoid fitting the spectra, rather 190 it has been simulated. To show that the intensity of 191 the CEF excitation peak at  $\sim 8.85$  meV is coming from <sup>192</sup> Pr<sup>3+</sup> ions, we have compared the intensity fall with the <sup>193</sup> calculated magnetic form factor of Pr<sup>3+</sup>, see Fig. 4(a).

TABLE I. Calculated CEF parameters from PC model with the effective charge  $2e/\mathcal{O}$  except the  $3^{rd}$  column.

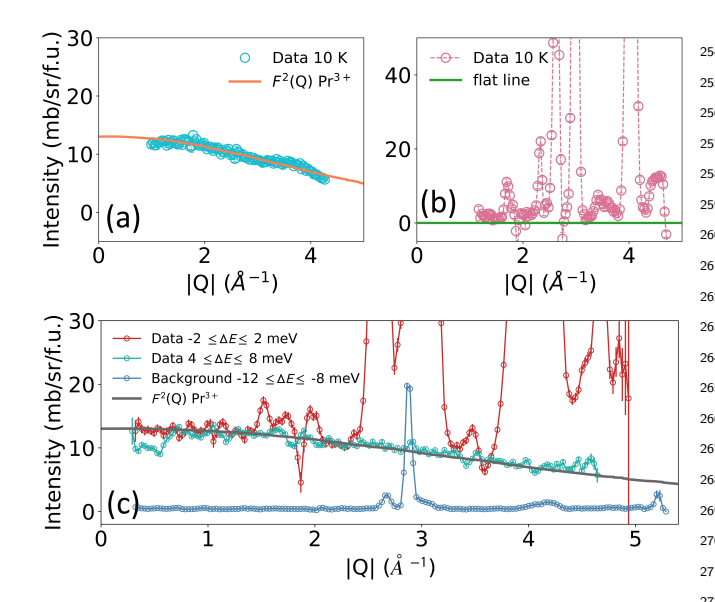
$B_n^m \text{ (meV)}$	PSNO	PSNO	PNO	PNO
		(1.7e/O)	(no $O_{int}$ )	(with $O_{int}$ )
$B_2^0$	-1.0603	-0.9807	-1.4961	-0.8854
$B_2^1$				-8.2417
$B_2^2$			-0.1253	-0.0882
$B_4^0$	-0.0047	-0.0043	-0.0064	0.0003
$B_4^1$				0.0124
$B_4^2$			0.0021	0.0026
$B_4^3$				0.0978
$B_4^4$	0.0644	0.0595	-0.0578	-0.0361
$B_6^0$	9.204 e-05	8.514e-5	0.0001	0.0001
$B_6^1$				-0.0004
$B_{6}^{2}$			1.974 e-05	3.116e-05
$B_{6}^{3}$				-0.0004
$B_6^4$	0.0029	0.0027	-0.0027	-0.0038
$B_{6}^{5}$				-0.0023
$B_{6}^{6}$			8.157e-05	9.856e-05



(a) The INS spectra of PNO measured at MAPS spectrometer with incident neutron energy  $E_i = 60 \text{ meV}$  at 5 K and the corresponding 1D line cuts at (100) with 0.95  $\leq \Delta h \leq 1.05$  (r.l.u) are shown in (b) with vertical error bars, where the solid lines represent the calculated CEF excitations from the point charge (PC) model with two sets of CEF environment. Inverse magnetic susceptibility along the crystallographic (c) a- and (d) c-axis where the solid lines are the calculated susceptibility using PC models.

196 bility with the predicted CEF parameters and we have 197 found a fine agreement with the experiment shown in 198 Fig. 2(e,f). For the magnetic susceptibility, it should be 199 noted that the system contains two magnetic ions Pr<sup>3+</sup> 200 and Ni<sup>2+</sup>. Susceptibility  $(\chi_m)$  and the magnetization (M-H) curves of  $Pr^{3+}$  ion were calculated using an effective Hamiltonian  $\mathcal{H}_{CEF} + \mu_B g_J \mathbf{B.J}$  under the applied external magnetic field B. Calculated  $\chi_m^{-1}$  along the crystallographic c-direction reproduces adequately the experimental observation down to 5 K, whereas along a-axis a certain deviation occurs above 150 K, see Fig. 2(e,f). Such deviation comes from the Ni<sup>2+</sup> paramag-208 netic contribution since the Ni<sup>2+</sup> spin-stripe ordering  $_{209}$  does not get fully established at this temperature. Below  $_{210}$  150 K more or less the features of  $\chi_m^{-1}$  comes from the  $^{211}$  crystal field of  $\mathrm{Pr^{3+}}$  ions and they do not order magnet-212 ically down to 10 K as verified in the excitation spectra 213 and calculation due to its crystal-field induced singlet 214 ground state.

Now, we switch to PNO sample where we have much 216 more complicated situation regarding CEF environ-217 ment. Figure 3(a-b) display the CEF excitations spectrum obtained at 5 K. The low energy CEF level is  $_{219}$  observed at  $\sim 6$  meV but with less FWHM  $\sim 4$  meV compared to PSNO sample. This might be due to the 221 absence of Sr disorder in PNO sample. First, we con-222 sidered the CEF environment of Pr without O<sub>int</sub> i.e. 223 with only nine oxygen atoms as ligands similar to Fig. 224 1 (left) but having 2-fold rotational axis along z in the orthorhombic  $d_{2h}$  symmetry where only 9 non-zero  $B_n^m$ However, to have a confidence on the calculated CEF 226 parameters are allowed. Using this particular setting parameters, we have calculated the magnetic suscepti- 227 with the  $B_n^m$  parameters listed in Table I, it gives rise



(a) Integrated intensity of the INS spectrum of PSNO over the energy range  $6 \le \Delta E \le 10$  meV in Fig. 2(a) where the orange solid line represents the calculated magnetic form factor of Pr<sup>3+</sup> ion. (b) Integrated intensity of the INS spectrum of PSNO around the elastic scattering line over the energy range  $-2 \le \Delta E \le 2$  meV where the flat green solid line is the eye guide to zero intensity. In both cases the intensity integration has been performed taking into account fixed  $-0.3 \le \Delta k \le -0.2$  along (h, -0.1, 0). Strong intense peaks in (b) are coming from Bragg scattering. (c) Integrated intensity of the INS spectrum of PNO over the energy range  $-2 \le \Delta E \le 2 \text{ meV (red)}, 4 \le \Delta E \le 8 \text{ meV}$ (cyan) and  $-12 \le \Delta E \le 8$  meV (blue), where the grey solid line represents the calculated magnetic form factor of Pr<sup>3+</sup> ion. The intensity integration has been performed taking into account fixed  $-0.3 \le \Delta k \le -0.2$  along (h, -0.1, 0).

 $_{228}$  to a strong peak at  $\sim$  6 meV but the calculated  $\chi_m$  $_{229}$  (green curves in Fig. 3(c-d)) using these  $B_n^m$  parameters does not reproduce the experimental  $\chi_m^{-1}$  curves. 231 To look for the reason behind such discrepancies be-232 tween the calculated and experimentally observed data 233 we have decided to include the  $O_{int}$  (Fig. 1 (right)) in 234 the calculation to represent Pr-CEF environment in a 235 better way. We have considered two sets of Pr-CEF. 236 The first set contains 9/4 Pr atoms out of 8 Pr atoms of  $_{237}$  the PNO unit cell which will have the  $\mathrm{O}_{int}$  in the CEF  $_{238}$  environment as the  $O_{int}$  will be shared by the nearby 4 239 Pr atoms independent of which Wyckoff postion is oc- $_{240}$  cupied by  $O_{int}$  and the second set contains rest 23/4 Pr 241 atoms which will have no  $O_{int}$  in the CEF environment. 242 This information is crucial as the relative intensity of the CEF excitation calculated per formula unit will depend on these two sets of Pr atoms which will be treated as an  $_{245}$  overall scale factor. However, we had to consider these 246 two Pr-CEF sets in our calculations separately and af-247 terwards we performed the weighted sum of calculated 248 spectra according to the overall scale-factor as the CEF 249 is after all a single-ion property. This avoids overesti-250 mating the CEF spectral intensity.

However, as it is easily noticeable in the Fig. 1 (right) that inclusion of  $O_{int}$  does not preserve the 2-fold rozsi tation along z-axis anymore even in the F112/m set-

ting rather reduces it to lower symmetry  $(c_1)$  which 255 gives 15 non-zero  $B_n^m$  parameters out of 26 total pa-256 rameters. Since the diagonal (110) mirror plane con- $O_{int}$  taining the  $O_{int}$  still exists, it eliminates the other total 258 of 11 imaginary  $B_n^m$  parameters. With this setting calculated CEF excitations give rise to a peak at  $\sim 0.25$ meV (blue curve in Fig. 3(b)). It is difficult to identify this peak from our INS measurements as it is near 262 the zero energy incoherent scattering. Nonetheless we 263 have obtained a satisfactory agreement with the measured  $\chi_m^{-1}$  using these two sets of Pr-CEF environment; with and without  $O_{int}$ , in Fig. 3(c,d). Red curves rep-266 resent the combined signal after considering the overall scale factor from both Pr-CEF sets. In addition to the |Q|-dependency of the excitation peak intensity at  $\sim$ 269 6 meV, the integrated intensity around the elastic line 270 follow the magnetic form factor of Pr<sup>3+</sup> as presented in 271 Fig. 4(c), indicating the possible existence of the lowest  $_{272}$  excited CEF peak at  $\sim 0.25$  meV as calculated whereas Fig. 4(b) shows no such |Q|-dependency in PSNO sam-274 ple indicating no such presence of CEF state close to

Additionally, we have carried out the calculation of 277 magnetization curves for the both PSNO and PNO sam-278 ples which are shown in Fig. 5(a,b) and Fig. 5(c,d) re-279 spectively. Only Pr sublattice magnetization obtained  $_{280}$  from PC model are shown. In the PSNO sample mag-281 netization curves show typical AFM signal up to 7 T 282 whereas in PNO sample there is a saturation like ten-283 dency at higher field. and this is more likely from Pr 284 atoms. For both samples, calculated magnetizations  $_{285}$  along c-axis follows nicely with the experimental data  $_{286}$  than that along a-axis. This also indicates that in the 287 ab-plane Ni sublattice magnetizations needs to be in-288 cluded in order to have better agreement with the ex-289 perimental data. However, magnetic susceptibility and 290 magnetization curves are highly anisotropic indicating  $_{291}$  the c-axis as an easy-axis for  $\mathrm{Pr}^{3+}$ . The single ion 292 anisotropy of Pr atoms in terms of 3D magnetization

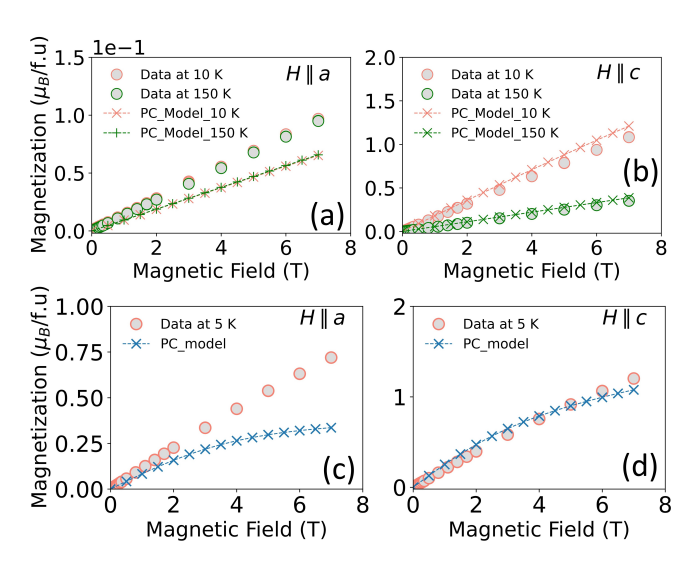


FIG. 5. Measured and simulated magnetization curves along the crystallographic a- and c-axes for the sample (a,b) PSNO and (c,d) PNO.

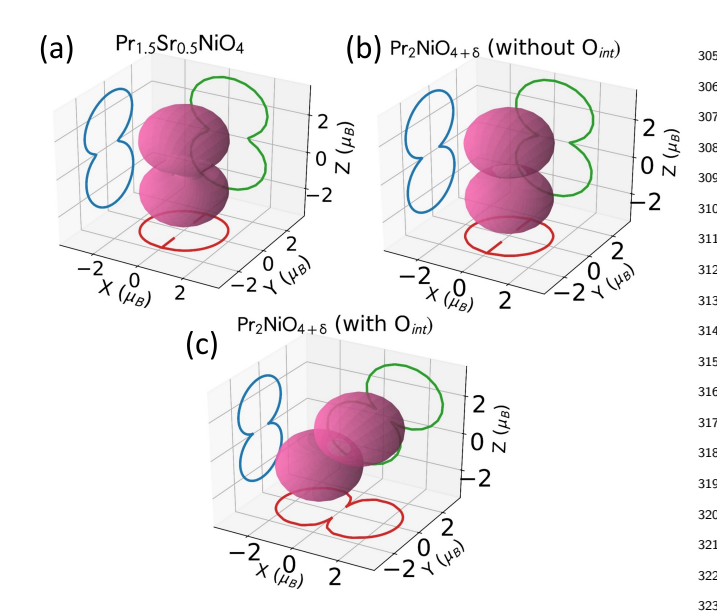


FIG. 6. 3D plots of saturation magnetization representing the Pr single ion anisotropies of PSNO and PNO, in various directions at 10 K computed from the CEF parameters using the field of 150 T. The colored traces indicate the outline of the 3D figure along the x, y, and z directions.

293 density distribution is calculated from the saturation 331 <sub>294</sub> magnetization using the CEF parameters listed in Ta- <sub>332</sub> ISIS Neutron and Muon Source Data Journal at [27]. <sub>295</sub> ble I for the PC calculation with 2e/O. The anisotropy <sub>333</sub> R. Dutta and A. Maity would like to acknowledge the 296 surfaces of magnetization for PSNO and PNO samples 334 support of Institut für Kristallographie, RWTH Aachen 297 are displayed in the Fig. 6. Figure 6(a) clearly indicates 335 Universität and Technische Universität München for 298 that the anisotropy surefaces for the PSNO sample is 336 supporting the travel expenses to perform the exper-299 pointing towards c-axis. For PNO sample the anisotropy 337 iments at MAPS, ISIS. We thank A. Scheie for the  $_{300}$  surfaces are treated separately (with and without  $O_{int}$ ).  $_{338}$  fruitful discussions on the point charge modeling using Without  $O_{int}$  the anisotropy surface in Fig. 6(b) is sim- 339 PYCRYSTALFIELD. Financial support from the French 302 ilar to the PSNO but including O<sub>int</sub>, Fig. 6(c) clearly 340 National Research Agency (ANR) through the project 303 shows the significant effect of the O<sub>int</sub> on changing the 341 SECTOR No. ANR-14-CE36-0006-01 is gratefully ac-304 anisotropy surface.

IV. Conclusion: In summary, crystal electric field excitations of Pr based 214-nickelates are investigated by using INS and macroscopic magnetization measurements where the effect of an interstitial oxygen in the O-doped sample has been revealed through CEF excitations in comparison with the Sr-doped sample. Our point charge models adequately reproduces the strong low-E CEF excitation peak in the INS spectrum for both sample. In addition, the calculated magnetic susceptibility together with magnetization curve based on CEF parameters indicate the nature of ground and excited states of Pr atoms depending on CEF environments. 317 Sr-disorder might accounts for the broadening of CEF  $_{318}$  excitations linewidth, in contrast ordered  $O_{int}$  may help 319 narrowing the linewidth of the CEF excitation in case 320 of O-doped sample. Additionally, from PC calculation 321 O-doping reveals a low-lying excited state near the zero 322 energy ground state which was necessary to interpret the 323 characteristics of susceptibility data. Inaddition, the ef- $_{324}$  fect of  $O_{int}$  on the anisotropy magnetization surfaces 325 is also revealed. Specially, this study highlights the importance of considering the both high and low symmetry  $_{327}$  Pr-CEF environments in the presence of  $O_{int}$ . Further 328 investigations on the CEF contribution from Ni octahe-329 dra relatively at high energy (> 100 meV) might benefit 330 such study.

ACKNOWLEDGEMENTS: MAPS data are available at 342 knowledged.

[1] E. S. Clementyev, P. A. Alekseev, V. V. Efimov, 364 I. O. Troyanchuk, A. S. Ivanov, V. N. Lazukov, 365 and V. V. Sikolenko, Crystal electric field effects in 366 Pr<sub>0.5</sub>Sr<sub>0.5</sub>CoO<sub>3</sub>, Journal of Surface Investigation. X-ray, <sup>367</sup> Synchrotron and Neutron Techniques 6, 553 (2012).

368

343

344

345

346

347

348

350

351

352

353

354

355

356

358

359

360

361

362

363

- A. Bhattacharyya, D. T. Adroja, A. M. Strydom, A. D. 369 Hillier, J. W. Taylor, A. Thamizhavel, S. K. Dhar, W. A. 370 Kockelmann, and B. D. Rainford, μSR and inelastic neutron scattering investigations of the noncentrosymmet- 372 ric antiferromagnet CeNiC<sub>2</sub>, Phys. Rev. B **90**, 054405 373 (2014).
- A. J. Princep, D. Prabhakaran, A. T. Boothroyd, and 375 D. T. Adroja, Crystal-field states of Pr<sup>3+</sup> in the candidate quantum spin ice Pr<sub>2</sub>Sn<sub>2</sub>O<sub>7</sub>, Phys. Rev. B 88, 104421 (2013).
- Z. Jirák, J. Hejtmánek, K. Knížek, M. Maryško, 379 P. Novák, E. Šantavá, T. Naito, and H. Fujishiro, 380 Ground-state properties of the mixed-valence cobaltites 381  $Nd_{0.7}Sr_{0.3}CoO_3$ ,  $Nd_{0.7}Ca_{0.3}CoO_3$  and  $Pr_{0.7}Ca_{0.3}CoO_3$ , 382 Journal of Physics: Condensed Matter 25, 216006 383 [10] (2013).

- [5] P. G. Freeman, A. T. Boothroyd, D. Prabhakaran, and J. Lorenzana, Magnetization of  $La_{2-x}Sr_xNiO_{4+\delta}$  (0  $\leq$  $x \leq 0.5$ ): Spin-glass and memory effects, Phys. Rev. B **73**, 014434 (2006).
- [6] L. M. Helme, A. T. Boothroyd, R. Coldea, D. Prabhakaran, C. D. Frost, D. A. Keen, L. P. Regnault, P. G. Freeman, M. Enderle, and J. Kulda, Magnetic order and dynamics of the charge-ordered antiferromagnet  $La_{1.5}Sr_{0.5}CoO_4$ , Phys. Rev. B **80**, 134414 (2009).
- J. M. Tranquada, Topological doping and superconductivity in cuprates: An experimental perspective, Symmetry 13, 10.3390/sym13122365 (2021).
- J. M. Tranquada, Spins, stripes, and superconductivity in hole-doped cuprates, AIP Conference Proceedings **1550**, 114 (2013).
- M. Hundley, J. Thompson, S.-W. Cheong, Z. Fisk, and S. Oseroff, Specific heat and anisotropic magnetic susceptibility of Pr<sub>2</sub>CuO<sub>4</sub>, Nd<sub>2</sub>CuO<sub>4</sub> and Sn<sub>2</sub>CuO<sub>4</sub> crystals, Physica C: Superconductivity 158, 102 (1989).
- A. T. Boothroyd, A. Longmore, M. Castro, R. Burriel, and R. S. Eccleston, The magnetic states of R<sup>3+</sup> in

- R<sub>2</sub>NiO<sub>4</sub> (R = Pr, Nd), Journal of Physics: Condensed 422 385 Matter 9, 2275 (1997). 386
- Т. R. Sachidanandam, Yildirim, A. B. Harris, 424 [20] |11|387 Aharony, and O. Entin-Wohlman, Single-ion 425 388 anisotropy, crystal-field effects, spin reorientation tran-389 sitions, and spin waves in R<sub>2</sub>CuO<sub>4</sub> (R = Nd, Pr, and 427 390 Sm), Phys. Rev. B 56, 260 (1997). 391
- 392 [12] M. Földeáki, H. Ledbetter, and Y. Hidaka, Magnetic 429 susceptibility of Pr<sub>2</sub>CuO<sub>4</sub> monocrystals and polycrys- 430 tals, Journal of Applied Physics 70, 5736 (1991). 394
- 395 [13] X. Batlle, X. Obradors, and B. Martnez, Magnetic inter- 432 [22] actions, weak ferromagnetism, and field-induced transi- 433 396 tions in  $Nd_2NiO_4$ , Phys. Rev. B **45**, 2830 (1992).
- 398 [14] M. T. Fernández-Díaz, J. L. Martínez, J. Rodríguez- 435 [23] Carvajal, J. Beille, B. Martínez, X. Obradors, and 436 399 P. Odier, Metamagnetism in single-crystal Pr<sub>2</sub>NiO<sub>4</sub>, 437 400 401 Phys. Rev. B 47, 5834 (1993).
- M. T. Fernández-Díaz, J. Rodríguez-Carvajal, J. L. 439 402 [15] Martínez, G. Fillion, F. Fernández, and R. Saez-Puche, 440 403 Structural and magnetic phase transitions in Pr<sub>2</sub>NiO<sub>4</sub>, 41 404 Zeitschrift für Physik B Condensed Matter 82, 275 442 405 (1991).406
- 407 [16] J. Rodríguez-Carvajal, M. T. Fernández-Díaz, J. L. 444 Martínez, F. Fernández, and R. Saez-Puche, Structural 445 408 phase transitions and three-dimensional magnetic order- 446 409 ing in the Nd<sub>2</sub>NiO<sub>4</sub> oxide, Europhysics Letters (EPL) 410 **11**, 261 (1990). 411
- A. Boothroyd, S. Doyle, M. Kumar, D. Paul, and R. Os- 449 412 born, Crystal fields in  $Nd_{2-x}Sr_xNiO_{4+y}$ , Journal of the 450 413 Less Common Metals 164-165, 915 (1990). 414
- 415 [18] M. Castro, R. Burriel, J. Pérez, A. Boothroyd, A. Long- 452 more, and R. Eccleston, Crystal-field energy levels 453 [26] 416 on Pr<sub>2</sub>NiO<sub>4</sub> by inelastic neutron scattering and heat-417 capacity measurements, Physica B: Condensed Matter 455 418 **234-236**, 728 (1997), proceedings of the First European 456 [27] 419 Conference on Neutron Scattering. 420
- 421 [19] A. Maity, R. Dutta, and W. Paulus, Stripe dis-

- commensuration and spin dynamics of half-doped  $Pr_{3/2}Sr_{1/2}NiO_4$ , Phys. Rev. Lett. **124**, 147202 (2020).
- R. Dutta, A. Maity, A. Marsicano, J. R. Stewart, M. Opel, and W. Paulus, Direct evidence for anisotropic three-dimensional magnetic excitations in a hole-doped antiferromagnet, Phys. Rev. B **102**, 165130 (2020).
- 428 [21] A. Maity, R. Dutta, A. Marsicano, A. Piovano, J. R. Stewart, and W. Paulus, Magnetic excitations in longrange stripe-ordered  $Pr_2NiO_{4+\delta}$ , Phys. Rev. B **103**, L100401 (2021).
- O. Sobolev and T. P. Jitae, Puma: Thermal three axes spectrometer, Journal of large-scale research facilities 1 (2015).
  - R. A. Ewings, J. R. Stewart, T. G. Perring, R. I. Bewley, M. D. Le, D. Raspino, D. E. Pooley, G. Škoro, S. P. Waller, D. Zacek, C. A. Smith, and R. C. Riehl-Shaw, Upgrade to the maps neutron time-offlightchopper spectrometer, Review of Scientific Instruments **90** (2019).
  - R. Dutta, A. Maity, A. Marsicano, M. Ceretti, D. Chernyshov, A. Bosak, A. Villesuzanne, G. Roth, G. Perversi, and W. Paulus, Long-range oxygen ordering linked to topotactic oxygen release in  $Pr_2NiO_{4+\delta}$ fuel cell cathode material, J. Mater. Chem. A 8, 13987 (2020).
  - [25] A. Maity, R. Dutta, O. Sendtskyi, M. Ceretti, Lebranchu, D. Chernyshov, A. Bosak, and W. Paulus, Exploring fast room temperature oxygen diffusion in  $Pr_2NiO_{4+\delta}$  stand-alone single-crystalline electrodes, Chemistry of Materials 34, 414 (2022), https://doi.org/10.1021/acs.chemmater.1c03847.

447

- A. Scheie, PyCrystalField: software for calculation, analysis and fitting of crystal electric field Hamiltonians, Journal of Applied Crystallography 54, 356 (2021).
- https://doi.org/10.5286/isis.e.rb1920233-1, (2019).